A manufacturability evaluation of complex architectures by laser powder bed fusion additive manufacturing

Martine McGregor[a],[**], Sagar Patel[a],[*], Kevin Zhang[a], Adam Yu[b], Mihaela Vlasea[a], Stewart McLachlin[a]

[a]University of Waterloo, Department of Mechanical and Mechatronics Engineering, Waterloo, ON N2L 3G1, Canada
[b]University of Waterloo, Department of Systems Design Engineering, Waterloo, ON N2L 3G1, Canada

Abstract

Additive manufacturing (AM) enables new possibilities for the design and manufacturing of complex metal architectures. Incorporating lattice structures into complex part geometries can enhance strength-to-weight and surface area-to-volume ratios for valuable components, particularly in industries such as medical devices and aerospace. However, lattice structures and their interconnections may result in unsupported down-skin surfaces, potentially limiting their manufacturability by metal AM technologies, such as laser powder bed fusion (LPBF). This study aimed at examining the correlation between down-skin surface area and the manufacturability of lattice structures fabricated using LPBF. Image processing algorithms were used to analyze down-skin surface areas of seven unique lattice designs and to devise quantitative metrics (such as down-skin surface area, discrete surface count, surface interconnectivity, down-skin ratio, over-print/under-print volumes, etc.) to evaluate LPBF manufacturability. The seven lattice designs were subsequently manufactured using maraging steel via LPBF, and then examined using imaging using X-ray micro-computed tomography (XCT). The geometric accuracy of the lattice designs was compared with XCT scans of the manufactured lattices by employing a voxel-based image comparison technique. The results indicated a strong relationship between down-skin surface area, surface interconnectivity, and the manufacturability of a given lattice design. The digital manufacturability evaluation workflow was also applied to a medical device design, further affirming its potential industrial utility for complex geometries.

Keywords: Additive manufacturing, Manufacturability, Powder bed fusion, Lattice structures, Design

1. Introduction

Metal additive manufacturing (AM) facilitates new possibilities for complex part geometry design and fabrication [1, 2]. Within metal AM, laser powder bed fusion (LPBF) is commonly used for industrial part production due to superior part resolution [3] and adaptability to different material

---

[*]Martine McGregor and Sagar Patel contributed equally to this article
[**]Corresponding author, Martine McGregor, m7mcgregor@uwaterloo.ca

types [4]. Despite these advantages of LPBF, limitations remain with respect to support structure requirements resulting in surface roughness, post-processing requirements, and material waste. Support structures are typically required on downward facing (down-skin) surfaces having angles with respect to the build plate between 0-45 degrees [5]. These down-skin surfaces, present in almost all parts designed for metal AM, require support structures for part anchoring and for thermal dissipation to mitigate the risk of excessive material vaporization and distortion due to residual stresses [6]. Unsupported down-skin may lead to increased surface roughness, deviations in part geometry, porous flaws, print failures and reduced mechanical performance [7]. Design considerations for down-skin surfaces, such as refinement and reduction of down-skin features with respect to part orientation to the build plate, need to be addressed prior to fabrication via LPBF. It can be challenging to completely minimize the occurrence of down-skin surfaces from components with complex architectures such as interconnected lattice structures with repeating down-skin surfaces [5].

Many complex parts in AM incorporate lattice architectures, a form of hierarchical design structures, to improve strength-to-weight and surface area-to-volume ratios through fine-tuning design parameters. Lattice structures vary widely in design and may be homogeneous or heterogeneous, surface or strut-based, and/or periodic or stochastic [5, 8, 9]. Lattices can be further classified as homogeneous or heterogeneous. Homogeneity (constant) versus heterogeneity (changing) in lattices refers to the thickness of unit cell features such as struts and/or walls [5]. Surface-based lattices, such as triply periodic minimal surface (TPMS) lattices, have a greater surface area-volume ratio than strut-based lattices, making them more suited for applications related to heat exchange, filtration, and biomedical devices wherein osseointegration is important. Strut-based lattices allow for higher strength and stiffness for structural components or load-bearing applications [10].Periodic lattices are comprised of a series of repeating unit cells, whereas stochastic lattices are random in nature. For high-value components like medical devices, the benefits of utilizing lattice structures within complex part geometries include light-weighting parts through topology optimization, controlling fluid flow, and tailoring biomimetic performance requirements for the human body [5, 11, 12, 13]. Such lattice structures are challenging to manufacture through traditional manufacturing methods due to their geometric complexity [10]. AM offers the adaptability required to produce these valuable metamaterials, independently or integrated as part of larger part geometries. However, lattice structures often have down-skin regions that cannot be supported adequately in LPBF due to the interconnectivity of the design features, making removal of support structures nonviable.

The angle between a given polygonal cell element and the build plate is referred to as the surface angle. Polygonal cell elements were then defined as features with a surface angle between 0 and 90 degrees, where 0-degree features are parallel to the build plate and 90-degree surfaces are perpendicular to the build plate. Polygonal cell elements with a surface angle below 45 degrees, termed down-skin

surfaces, are of particular interest to the AM community due to well-recognized manufacturability challenges. Side-skin surfaces and up-skin surfaces, are polygonal cell elements with a surface angle between 90-180 degrees and are generally considered manufacturable with LPBF technologies and were excluded from analysis in this study.

The quality of down-skin surfaces in LPBF components has been previously examined in literature. It is well established that surfaces between 0-45 degrees to the build plate are prone to poor geometric fidelity and dross, or over-printing, the phenomenon in which partially sintered powder fuses to solid surfaces resulting in increased surface roughness [14, 15, 16, 17]. Meanwhile under-printing, the absence of material with respect to CAD parts, can be caused in LPBF parts by the porous powder melting and then rapidly solidifying [18, 19]. Print parameters have been found to affect the manufacturability of down-skin surfaces through experiments examining surface angle, scanning speed, laser power, accumulated residual stress, and scanning vector length [20, 21, 22]. Laser scanning strategies can also be controlled through tailored algorithms to improve surface roughness and reduce geometric variation on down-skin surfaces [23]. Down-skin surfaces have also been shown to increase near-surface porous defects in LPBF parts [24, 25]. In an intensive experimental investigation, Shange et al. [24] reported an inversely proportional relationship between down-skin surface angle and near-surface porosity and surface roughness, with a lower down-skin angle being associated with greater near-surface porosity and surface roughness. Design for additive manufacturing tools for the design of lattice structures have been established in efforts to optimize strut element shape and orientation [26]. These studies show that there is an overall interplay between process parameters and design that often require significant optimization efforts to ensure manufacturability and geometric fidelity.

Measuring part tolerance and geometric accuracy is an important aspect of understanding part quality and evaluating manufacturability. Historically, the geometric accuracy of parts has been measured from two-dimensional (2D) cross-sections at features of interest; this technique has been successfully used to complete complex part geometry investigations [27]. Through 2D measurement of part geometry, information concerning over-printing and under-printing of specific regions can be obtained. This is often how dross, or over-printing of down-skin surfaces, is measured. Over-printing and under-printing can also be measured volumetrically through analysis of the total part by weight, volume displacement, or X-ray computed tomography (XCT) images [28, 29, 30]. While these techniques provide insight into the overall success of the manufactured part, there are few tools that include evaluation of localized over- and/or under-printing [31].

Down-skin surfaces remain a difficult challenge for AM using LPBF, especially for complex interconnected lattice geometries where down-skin support is typically not feasible. The primary goal of this work is to develop digital evaluation tools to identify how and where down-skin surfaces are likely to fail within lattice structures produced through LPBF. This was completed by evaluating

the angle, the degree of interconnectivity, and surface area of down-skin surfaces within a lattice structure against outcomes from manufactured parts. To achieve this task, digital tools were developed to quantitatively assess manufacturability outcomes for different lattice types. Evaluation was done relative to down-skin characteristics by examining pore flaws and 3D geometric part divergence between ideal computer-aided designs (CAD) and manufactured parts digitally reconstructed via XCT. It was hypothesized that down-skin characteristics such as surface area and interconnectivity would correlate to geometric deviations in lattice structures produced through LPBF.

Following the evaluation of the marging steel lattice structures, the manufacturability evaluation workflow was then applied to an example orthopaedic implant design featuring lattice structures. The orthopaedic implant was manufactured in Ti6Al4V in order to highlight the adaptability and applicability of the developed tool. The aim of the present work is to provide a new digital tool to better quantify the three-dimensional (3D) geometric fidelity of complex parts produced using AM at the design stage.

2. Methodology

2.1. Design and evaluation of lattice structures

Seven unique homogeneous periodic lattices were designed to evaluate the effect of down-skin surface characteristics on manufacturability: face-centred cubic (FCC), body-centred cubic (BCC), graphical diamond, octet, TPMS gyroid, TPMS Schwarz, and TPMS diamond. The seven periodic lattice structures were designed using the nTopology software (nTopology Inc., New York, NY). Lattice geometries were used to fill a 20 x 20 x 20 mm cubic design space, with a homogeneous lattice. The wall thicknesses or strut thicknesses of CAD lattices were designed to 1 mm thick, as shown in Figure 1. For the seven periodic lattices, a unit cell size of 10 x 10 x 10 mm was used.

2.2. Evaluation of down-skin

To further understand the impact of surface angle on geometric fidelity of final parts, a custom Python software tool was developed using 3D Slicer (v.4.11) to determine localized surface angles from the CAD models of the different lattice types. 3D Slicer uses the open-source Visualization Toolkit (VTK) for polygonal representation of CAD models from STL files. Two VTK classes, namely vtkPolyDataNormals and vtkMath, were leveraged in the custom Python script to determine the surface angle of individual polygon cell elements relative to a set normal plane. The normal plane in this case was set to match the LPBF build plate plane to determine the relative surface angle of polygon cells within the lattice structures. The calculated surface angles were then applied to each polygonal cell element as an associated scalar value.
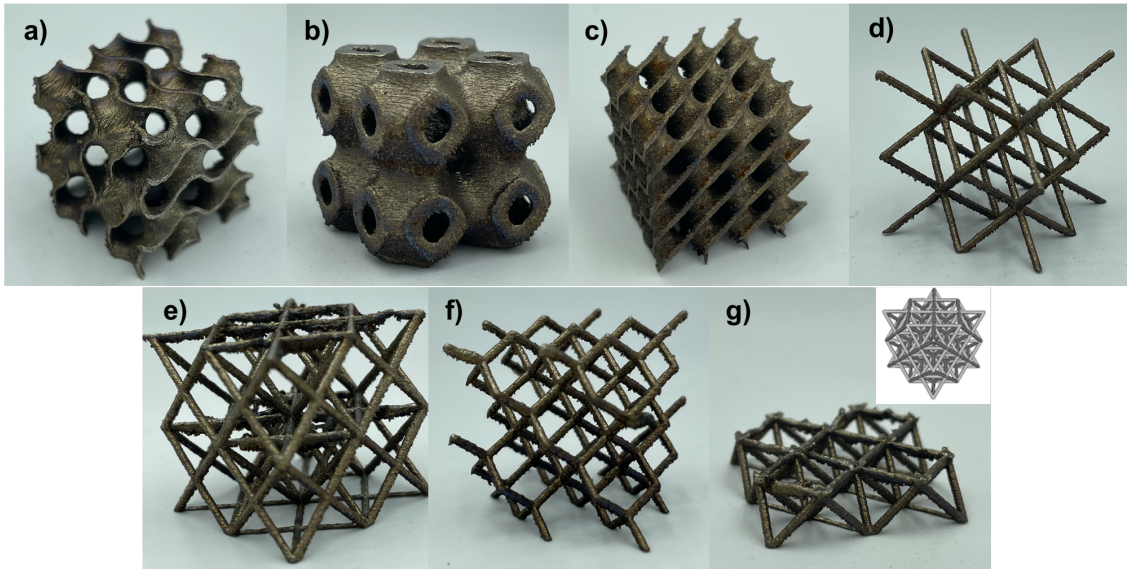
4

Figure 1: Seven unique homogenous lattice structures were printed using maraging steel through laser powder bed fusion (M290, EOS, Germany): (a) TPMS gyroid, (b) TPMS Schwarz, (c) TPMS diamond, (d) body-centred cubic, (e) face-centred cubic, (f) graphical diamond, and (g) octet (failed).

With this approach, the normal plane, or build plate, has a unit normal of [0, 0, 1] in Cartesian coordinates. The angle between the auto-oriented (outward-facing) unit normal of each polygon cell and the build plate normal was calculated to obtain the surface angle of each triangular mesh element. To better visualize surface angles within the lattice structures, down-skin surfaces were discretized into 15-degree surface angle increments and assigned a colour. The 15-degree discretization value was selected based on a balance between discretization of down-skin regions for visualization and analysis, prior manufacturability and surface quality challenges reported in literature [32, 33, 34, 35], and observed by the authors through experience. Within each 15-degree increment bin, up to 90 degrees orientation, the total down-skin surface area and percentage of total down-skin surface per increment bin were calculated. Down-skin surfaces in contact with the build plate were excluded from surface area calculations, as these surfaces are supported during the LPBF manufacturing process and therefore do not pose the same challenges as unsupported down-skin surfaces.

2.3. Manufacturing and evaluation of manufacturability

The seven homogeneous lattice structures were manufactured with 18Ni-300 maraging steel (Böhler, Germany) using metal AM via LPBF (M290, EOS, Germany). The beam spot diameter of the EOS M290 LPBF system used was 90 µm, which was kept constant for the study. A hard recoater was utilized in this study. The maraging steel powders were gas atomized with a nominal particle size range of 15-43 µm. All the lattice structures were part of the same print. The LPBF print parameters were tailored

for complex parts and thereby included different process parameters for the core, contour/border, down-skin, and up-skin based on a previously developed recipe for maraging steel, and are summarized in Table 1. One contour was used for printing all the lattice structures. If a given lattice was protruding above the powder bed before recoating of the next layer of powder, this posed a potential risk of damage to the recoater and therefore raised edges on the build plate were used as visual inspection criteria.

Table 1: Summary of the LPBF print parameters for the nine lattice structures using 18Ni-300 maraging steel on EOS M290 that include: core, contour, down-skin and up-skin parameters. *Note that contour is printed first, then core.

Parameter	Core	Contour*	Down-skin: core & contour*	Up-skin: core & contour*
Power	370 W	321 W	100 W	325 W
Velocity	0.92 m/s	0.74 m/s	1 m/s	1m/s
Hatch distance	0.1 mm	N/A	0.1 mm	0.1 mm
Beam offset	0.05 mm	0.05 mm	N/A	N/A
Hatch rotation	67°	N/A	90°	90°
Overlap with core	N/A	N/A	0.08 mm	0.08 mm
Strategy	Meander	N/A	Meander	Meander
Layer thickness	0.04 mm	N/A	4 layers	2 layers

2.3.1. Evaluation of part porosity

Following manufacturing, the nine lattice structures were removed from the LPBF build plate using electro-discharge machining (EDM) and were then imaged using an XCT scanner (ZEISS Xradia 520 Versa) for non-destructive evaluation of manufacturing outcomes. A voxel size of 30 µm was used for scanning each lattice structure, captured in a single field of view. An image processing software was used to complete porous flaw and geometric fidelity detection and visualization (Dragonfly 3.0, Object Research Systems Inc., Montreal, QC) and MATLAB (version 9.1). Lattice structures were imported into the imaging software and subjected to a greyscale threshold allowing for segmentation between the solid material and porous flaws. Segmentation results were then binarized, and resulting images were used to characterize porous flaws based on aspect ratio. Porous flaws with an aspect ratio greater than or equal to 0.7 were considered rounded (spherical) flaws and porous flaws with an aspect ratio lesser than 0.7 were considered irregularly shaped flaws. The porous flaws within the XCT data volume were then highlighted through manual adjustment of brightness, contrast and opacity. Boolean operators were used to compare the porous flaw to solid material ratio to determine overall print porosity.

2.3.2. Measurement of geometric accuracy

A voxel-based comparison method was used to assess the geometric fidelity of the printed parts compared to the original CAD models. The CAD design file for each lattice structure was segmented into a stack of black and white images, with a 30 µm voxel size to match the voxel size resolution from the XCT characterization. This allowed for the data to be represented as arrays of Boolean values, with the presence of material being denoted 1/white and material not present being denoted 0/black. A custom Python script was then developed and employed to compare the CAD and XCT datasets voxel by voxel. Two measures of print inaccuracy were used: over-print and under-print. The over-print percentage was defined by the total number of voxels in which the XCT data returned material present and the CAD geometry returned no material present, normalized by the total number of CAD voxels. Conversely, the under-print percentage was the number of voxels in which the CAD returned material present but the XCT data did not, again normalized by total CAD volume. The under-print percentage includes the presence of pores, which are a contributing factor to assessing a printability criteria. These metrics were evaluated both as a total value across the entire part and on a slice-by-slice basis (corresponding roughly to each print layer), in order to produce a more specific understanding of volumetric and local accuracy for the lattice structures. To obtain the layer-by-layer metrics, the over- and under-print values were normalized by the CAD volume for each layer.

Further, the porosity fraction and actual mass to CAD mass estimation ratio for the six successfully manufactured homogeneous periodic lattice structures were determined. Porosity fraction was obtained through µCT imaging. Actual part mass of the final parts was measured with a micro resolution scale and compared to the estimation given by the nTopology software.

2.3.3. Workflow adaptability for end-use product design

In addition to the maraging steel cubic lattice structures, two Ti6Al4V orthopaedic implant designs were manufactured on the same EOS M290 LPBF system using a set of previously optimized processing parameters [36]. The two implants were also evaluated with the digital evaluation workflow to assess the adaptability of the workflow for industry applications. Additionally, the use of another material and a stochastic lattice design for these products helps determine the material and design independence of this workflow for LPBF. Both orthopaedic implants had the same outer geometry. However, the internal part was light-weighted with two different lattice structures: TPMS gyroid and Voronoi. The TPMS gyroid lattice was selected as it successfully manufactured in the first stages of the study. The Voronoi lattice was selected for its novelty and ability to assess further potential of the digital evaluation workflow. Final implant designs are visualized in Figure 8 in Section 3.2.1. Evaluation of the down-skin distribution, measurement of part porosity and geometric accuracy were then performed for the orthopaedic implants to evaluate the adaptability and applicability of the digital evaluation

workflow for end-use products.

3. Results

Only five of the seven lattice structures were considered to be successfully manufactured in maraging steel through LPBF. The BCC, graphical diamond, TPMS gyroid, TPMS Schwarz, and TPMS diamond all were successfully printed and were available for further evaluation. The FCC lattice printed in full and was XCT imaged for analysis; however, it had significant part defects and was considered a print failure by visual inspection.The octet lattice structure suffered major print failures and was cancelled during the LPBF printing process (Figure 1). Therefore, it was omitted from the porous flaw and geometric accuracy analyses.

3.1. Evaluation of down-skin surfaces

The down-skin spatial distribution for the seven unique lattice structures was determined using the custom pipeline developed in section 2.1. The down-skin angle for the surface of each lattice structure was discretized into 15-degree increments; the results of this discretization are shown in Figure 2. The FCC and octet lattices had the highest percentage of down-skin surfaces with a surface angle below 30 degrees with 11.07% and 11.47% respectively, as visualized in Figure 3.

In addition, the interconnectivity of down-skin regions was examined to determine the number of discrete down-skin features with a surface angle between 0-15 degrees. From this discrete down-skin feature calculation step, a down-skin ratio was defined in Equation 1 that is given by the total surface area with 0-15 degrees surface angle divided by the number of discrete down-skin features with a surface angle of 0-15 degrees to the build plate.

$$\text{Down-skin ratio} = \frac{\text{Surface area with 0-15 degrees surface angle}}{\text{Number of discrete down-skin features with 0-15 degrees surface angle}} \quad (1)$$

The interconnectivity of down-skin surfaces with a down-skin angle between 0-15 degrees was quantified by the down-skin ratio method. The down-skin ratio was calculated for all the lattice structures in Table 2. It was found that the lattice structures that printed successfully had a down-skin ratio of less than ($<$) 1, whereas lattice structures that failed to print had a down-skin ratio greater than ($>$) 1. An illustration of the interconnectivity of such 0-15-degree down-skin surfaces is illustrated for select lattices as shown in Figure 4.

3.2. Evaluation of manufacturability

Porous flaw types, irregular or round, were also visualized. Few porous flaws were visible within the lattice structures, which may be attributed to the coarse resolution of the XCT. As an illustration, the

Lattice	Top isometric view	Bottom isometric view	Front view	Color	Downskin angle
TPMS gyroid					0-15°
TPMS Schwarz					15-30°
TPMS diamond					30-45°
Body centered cubic					45-60°
Face centered cubic					60-75°
Graphical diamond					75-90°
Octet					90°+

Figure 2: Seven unique homogeneous lattice structures were evaluated for down-skin regions ranging from 0 to 90 degrees of down-skin in 15-degree increments: TPMS gyroid, TPMS Schwarz, TPMS diamond, body-centred cubic, face-centred cubic (partially failed), graphical diamond, and octet (failed).
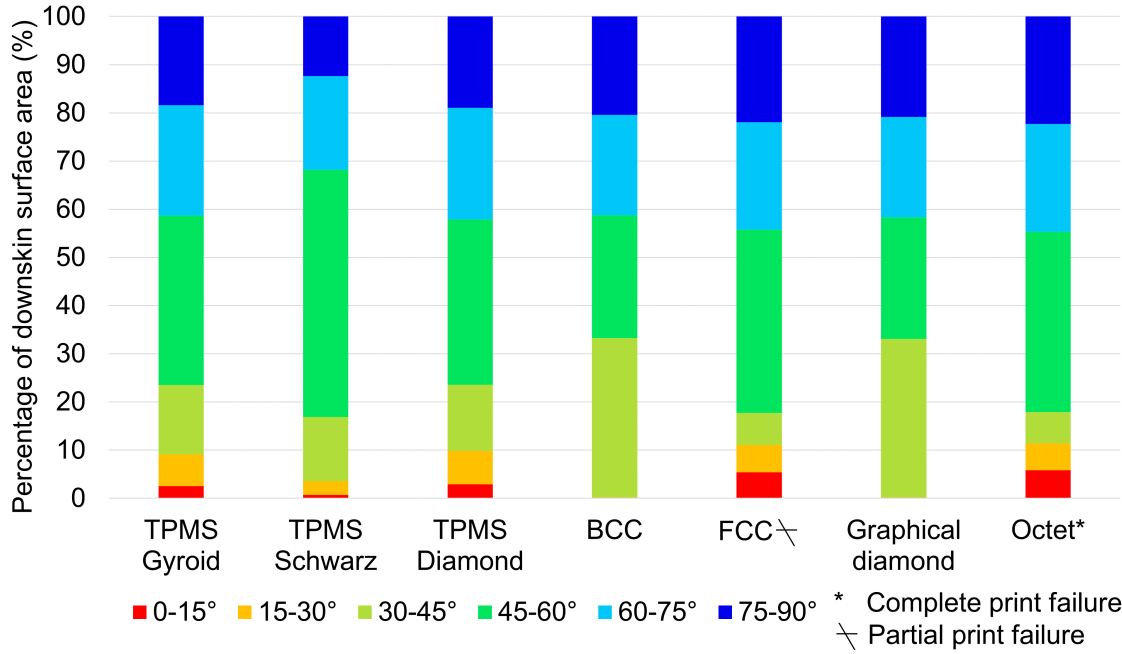
Figure 3: Down-skin distribution as determined using the custom 3D Slicer algorithm and discretized into 15º increments. Amongst the seven homogeneous lattice structures, FCC and octet lattices have the highest percentage of down-skin surfaces with an angle $<30º$ at 11.07% and 11.47% respectively.

Table 2: Calculated values of the surface area of down-skin features, number of discrete down-skin features, and down-skin ratio for the seven homogeneous periodic lattice structures manufactured using LPBF in this study.

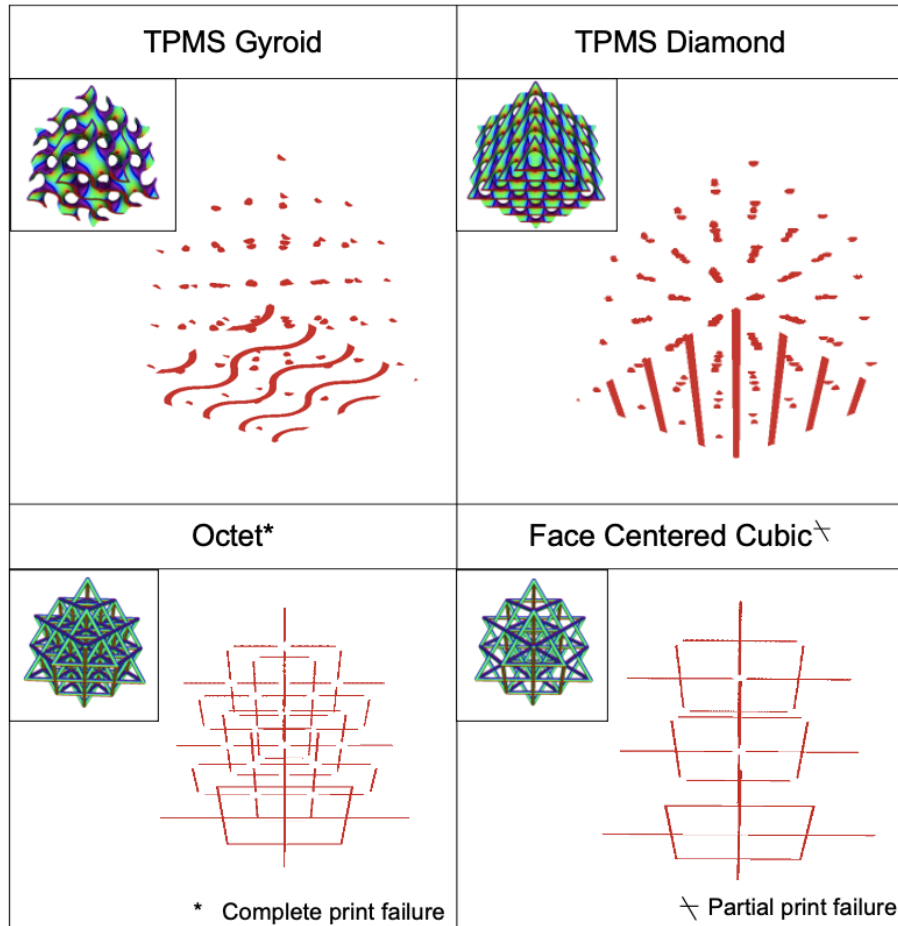| Lattice structure	Surface area of down-skin features $<15°(mm^2)$	Number of discrete down-skin features $<15°$	Down-skin ratio $(mm^2/\text{no. of}$ features)
TPMS gyroid	62.4	80	0.78
TPMS Schwarz	12.1	48	0.25
TPMS diamond	89.5	128	0.70
BCC	0.54	9	0.06
FCC	82.1	65	1.26
Graphical diamond	0.78	13	0.06
Octet	119.0	9	13.22

Figure 4: A bottom isometric view of lattice down-skin is provided. Enlarged (1:3), discrete down-skin regions with an angle of 15 degrees or less to the build plate (red) were isolated with the aim of better understanding the effect of down-skin area and interconnectivity of discrete down-skin features on printability challenges. Complete lattice structures with down-skin visualization were included for each lattice to provide context for the discrete down-skin regions. The discrete down-skin features for the TPMS gyroid (top left), TPMS diamond (top right), octet (bottom left) and face-centred cubic (bottom right) lattice structures are visualized above.

XCT of the TPMS Schwarz lattice can be seen in Figure 5, where irregular porous flaws are in blue and round porous flaws are in red. Those porous flaws present, were clustered along the down-skin regions of the parts as previously shown by Shange et al. [24]. The qualitative pore visualization is further confirmation that porous flaws are closely related to the interplay between process parameters and the design in the down-skin region.
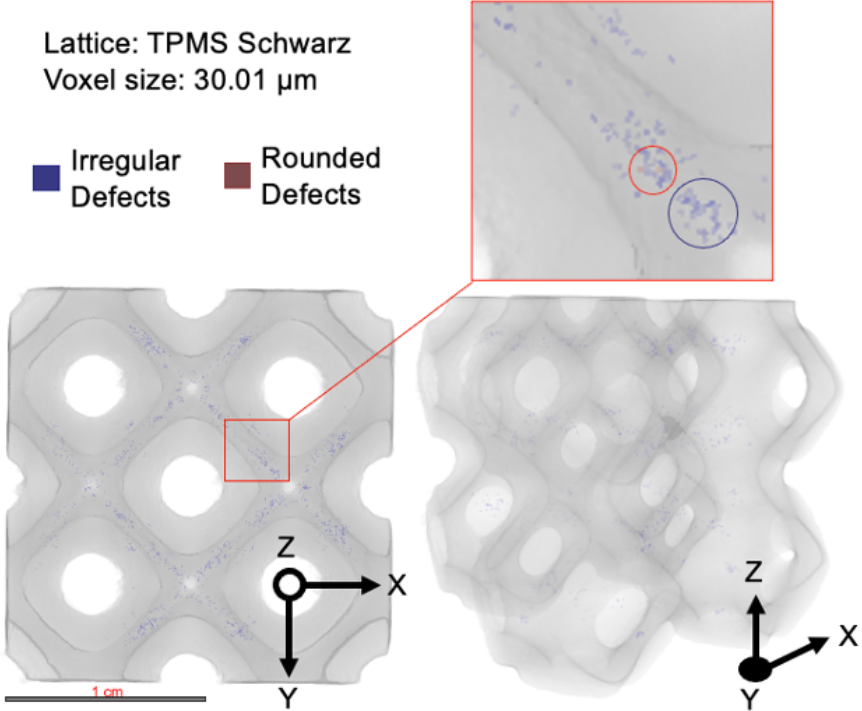

Figure 5: An X-ray computed tomography image of a maraging steel TPMS Schwarz lattice structure produced with laser powder bed fusion is visualized in frontal (left) and isometric (bottom right) views. An enlarged section (upper right) allows for visualization of irregular (blue) and round (red) porous defects to depict the prevalence and location.

The seven lattice structures that were printed to completion were analyzed based on the over-print and under-print metrics described in section 2.3.2. The TPMS lattice structures printed more accurately to the design CAD than the strut-based lattices did, for both over-print volume and under-print volume, as captured in Table 3. In order to illustrate the relationship between surface angle and geometric print fidelity, the slice-by-slice over- and under-print data were aligned and compared. The TPMS gyroid and the FCC were used as examples from the surface-based and strut-based categories, respectively. Figure 6 shows that a small down-skin angle aligns with a peak in over-printing, while up-skin surfaces align with a peak in under-printing. These phenomena are more pronounced for the FCC lattice structure where large unsupported down-skin regions are present. The FCC lattice analysis shows two large

spikes in layer over-print, which correspond to the areas of zero-degree down-skin angle. Significant dross formation is visible on the superimposed XCT/CAD data, as seen in Figure 6 and for the FCC lattice in particular. Layer-by-layer comparisons of the XCT and CAD data for the remaining four successfully printed homogeneous periodic lattice structures are provided in Supplementary Information Figure 1.

Table 3: Total volumetric over-print and under-print evaluation using the CAD and XCT data of the eight successfully manufactured structures.

Lattice structure	Percent volume over-print (%)	Percent volume under-print (%)
TPMS gyroid	5.3	21.6
TPMS Schwarz	2.7	11.3
TPMS diamond	5.2	21.7
BCC	7.5	32.4
FCC	16.0	31.3
Graphical diamond	8.9	32.6
Interbody cage: gyroid	21.3	8.5
Interbody cage: Voronoi	30.2	13.0

To further understanding of the effect of the down-skin ratio on the manufacturability of the various lattice structures, Table 4 and Figure 7 provide a comparison of the average over-print and under-print between the CAD and XCT for all the eight successfully manufactured structures, with standard deviations provided for the slice-by-slice comparisons.

Table 4: Porosity fraction (of the CAD designs) and mass ratio (actual mass/CAD mass) for the six successfully manufactured homogeneous periodic lattice structures.

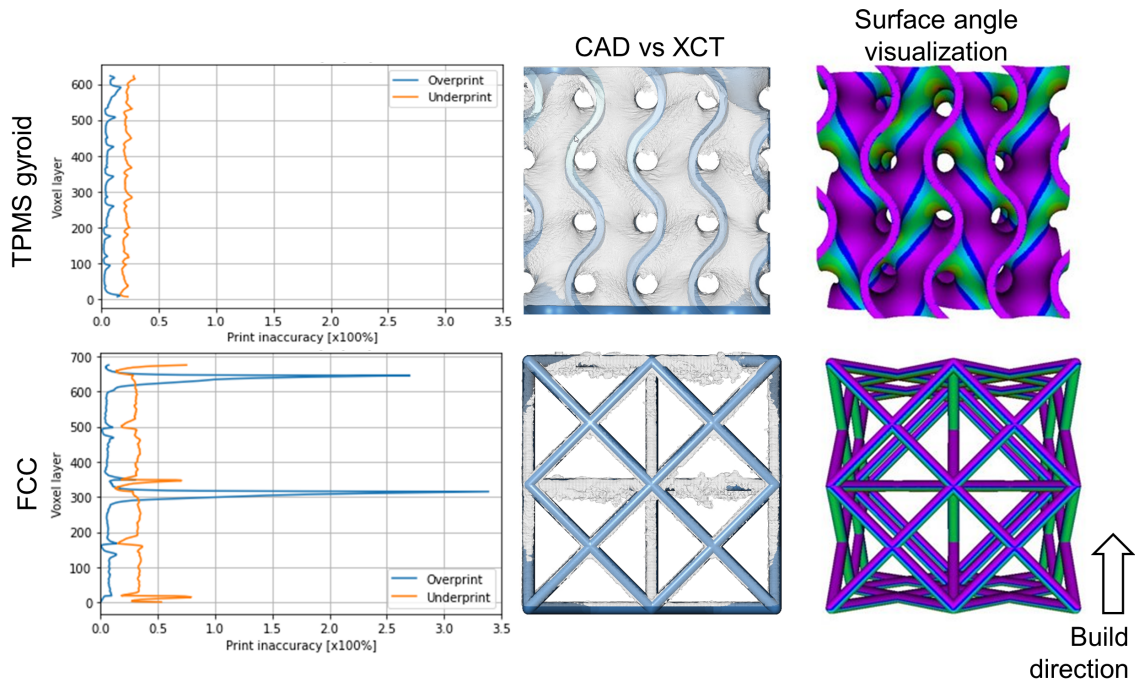| Lattice structure	Porosity fraction of CAD (%)	Ratio of actual mass (from XCT) over CAD mass (%)
TPMS gyroid	80.66	83.76
TPMS Schwarz	65.7	91.35
TPMS diamond	76.82	83.51
BCC	94.89	75.23
FCC	90.81	84.62
Graphical diamond	94.88	76.27

Figure 6: Surface-based lattices TPMS gyroid (top), were found to be more printable than strut-based lattices, FCC (bottom). The TPMS gyroid had 5.3% and 21.6% volumetric over- and under-print respectively, while the FCC had 16.0% and 31.3% (left). When aligning quantitative values for over-print and under-print to X-ray computed tomography (XCT) (middle) and surface angle (right), a clear association between down-skin surfaces and poor print quality becomes apparent.

3.2.1. Example applicability to an industrial application

The two orthopaedic implant designs had a greater percentage of total down-skin surface area under 15 degrees with respect to the build plate orientation when compared to most of the cubic lattice structures previously examined (as seen in Figure 8 (left)); however, they were considered manufacturable due to the large distribution of small discrete down-skin regions throughout the part, as indicated by a down-skin ratio of less than one (<1) and illustrated in Figure 8 (right). Layer-by-layer comparisons of the XCT and CAD data for the two implant structures are provided in Supplementary Information Figure 2, which shows the successful manufacturing of the two implant designs. From this it was seen that the down-skin ratio may help evaluate manufacturability in the design phase. However, it remains important to take other designs considerations into account such as shape of discrete down-skin regions, wall or strut thickness and aspect ratios to further ensure part manufacturability.

4. Discussion

Lattice type was the first factor taken into consideration when examining the overall manufacturability of complex lattice architectures with respect to the down-skin surface areas. Comparing the
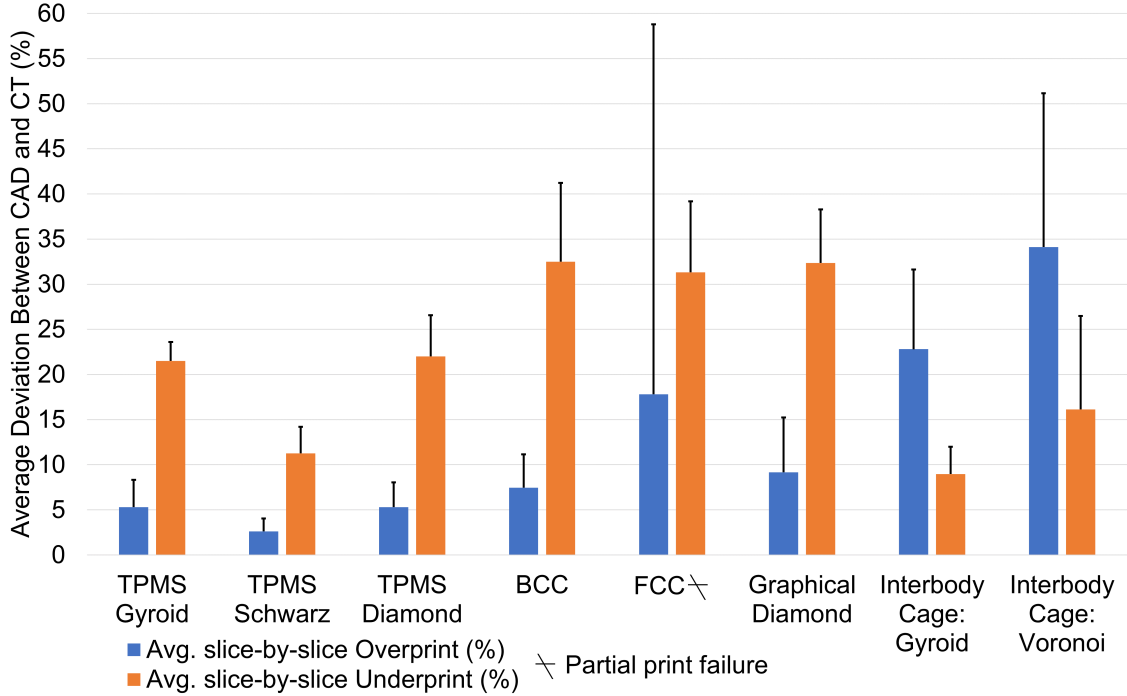
Figure 7: Average and standard deviations for volumetric over-print and under-print from slice-by-slice comparisons of the CAD and XCT data of the eight successfully manufactured structures.

strut-based lattices, the FCC and octet strut-based lattices have long struts whose central axis runs parallel to the build plate, unlike BCC and graphical diamond lattices, where strut elements are at a minimum of 45 degrees to the build plate. This leads to a significant amount of challenging down-skin surfaces with a surface angle below 15 degrees in the FCC and octet as evident in Figure 4. Surface features that were parallel to and touching the build plate were excluded from analysis. Excluding the failed FCC and octet lattices, the TPMS diamond and TPMS gyroid have the highest percentage of down-skin between 0 and 30 degrees, as shown in Figure 3. However, TPMS lattices (gyroid, diamond, and Schwarz) also have a significant amount of surface area touching the build plate and are all successfully manufactured using LPBF. This could be associated with the improved heat transfer to the solid metal on the LPBF build plate, when compared to printing on a powder bed which is known to have significantly lower thermal conductivity [37] and density [38].

The distribution of down-skin features (unsupported down-skin surfaces between 0-15 degrees) was also found to have an effect on the manufacturability of complex architectures. The TPMS gyroid lattice structure had 80 discrete features with a consistent surface angle between 0-15 degrees. Similarly, the TPMS diamond had 128 discrete features with a consistent surface angle between 0-15 degrees. However, the overall surface area for these down-skin features was relatively small for these lattice types, leading to a down-skin ratio of 0.78 and 0.70 for the TPMS gyroid and TPMS diamond,
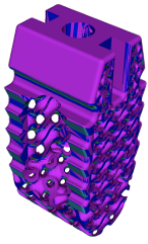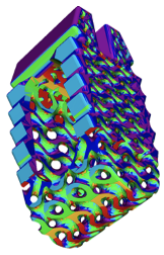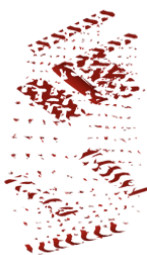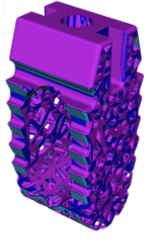
15
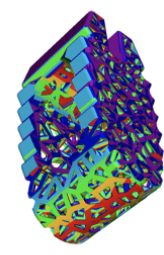
Design	Top isometric view	Bottom isometric view	Front view	Discrete surfaces <15º	Surface area <15º (mm²)	Downskin ratio
Interbody cage – gyroid					105.52	<1
Interbody cage - Voronoi					134.24	<1

Figure 8: (Left) Down-skin distribution within the complete orthopaedic implant parts was determined using a custom algorithm and discretized into 15-degree increments. Distribution for the TMPS gyroid and Voronoi cubic designs were included for comparison. (Right) The two light-weighted orthopaedic implants were evaluated for down-skin regions ranging from 0 to 90 degrees of down-skin in 15-degree increments.

respectively. The regions of interest in both lattices exhibit saddle-like geometry which has been shown to be suitable for additive manufacturing [39, 40]. The FCC and octet lattices had fewer but larger connected down-skin features between 0-15 degrees leading to a down-skin ratio of 13.22 and 1.26, respectively. These regions are not saddle-shaped and are located at the underside of struts, which are parallel to the build plate. A large surface area of unsupported down-skin features (0-15 degrees) likely contributes to manufacturability challenges for the FCC and octet lattice structures. It is known that stress accumulation occurs as the surface area of a given discrete region increases and thereby increasing the risk of defects [23]. Therefore, the down-skin ratio term proposed in this work may be a useful tool in digitally evaluating part manufacturability using AM as it provides a more comprehensive characterization of down-skin surfaces. A known limitation of this work-flow is the lack of consideration for "knife edge" features. These features would be captured as one discrete down-skin feature, thereby lowering the down-skin ratio. However, the small surface area associated with knife edge features would act to decrease the down-skin ratio. This relationship between low surface area for singular down-skin features with respect to the performance of the down-skin ratio is unknown and should be considered in future work.

As expected, among the homogeneous periodic lattice structures that printed, the FCC lattice

structure exhibits the highest average as well as highest standard deviation in terms of over-printing when the CAD and XCT data are compared. The high standard deviation in particular is related to the two large down-skin (0-15 degrees) features of the lattice structure that are shown to have volumetric over-print of ∼330% in the printed part as shown in Figure 6. These down-skin features within the FCC lattice structure are effectively parallel to the LPBF build plate which would typically require support structures for improving thermal conductivity [41], reducing part deformation [42], and preventing dross formation [21] in LPBF.

A relatively large volumetric under-print is observed in all of the homogeneous periodic lattice structures (Table 3 and Figure 7). For the TPMS lattices, the total volumetric under-print is between 11.3-21.7% as shown in Table 3. For the strut-based lattices, the total volumetric under-print is significantly higher when compared to the TPMS lattices (31.3-32.6%, as shown in Table 3). Overall, all lattices did under-print when compared to the designed CAD (75-91%), as shown by the ratio of the actual mass from XCT data to the CAD mass in Table 4. The under-printing observed in all lattices can be partly explained by shrinkage caused by the melting of porous powder followed by rapid solidification in LPBF, and has been reported for TPMS lattices in literature [18, 19]. Additionally, laser power [43], scanning speed [43], layer thickness [43], and build plate location of a given part [44] are other factors that could have effects on shrinkage [43].

Layer-by-layer specimen geometry is known to have significant effects on shrinkage as well [45] since it would directly influence the boundary conditions for the following layer, in the sense of whether or not a given feature in the current layer is supported by solidified metal or the powder bed, both of which have significantly different thermal conductivity values [37]. Porosity fraction for the surface-based (TPMS) and strut-based lattice designs in Table 4 can help understand the expected differences in layer-by-layer geometry. In Table 4, the porosity fraction of a given lattice structure design is calculated as $1 - Volume fraction$, wherein volume fraction denotes the volume of the lattice structure CAD divided by the volume of the solid cube model (20*20*20 mm^3). The porosity fractions of all strut-based lattice designs are >90% whereas the porosity fractions of all surface-based (TPMS) lattice designs are between 65-80%. The higher porosity fraction in strut-based lattice designs would mean that there is a higher probability that for a given feature in a given layer, the underlying boundary conditions are more likely to be driven by the poor thermal conductivity powder bed for strut-based lattices, when compared to the surface-based lattices. A powder bed driven boundary condition would mean that for strut-based lattices, the melted portions of a given layer would also be on a relatively low-density powder bed. This would lead to a higher volumetric over-print due to dross formation, as well as under-print due to shrinkage and potential distortion of the down-skining features due to poor thermal conductivity of the powder bed [46]. A higher porosity fraction in strut-based lattice designs, as shown in Table 4 is thereby expected to cause the high volumetric under-print and over-print observed in

Figure 7 and Table 3, as also reported by Taib et al. [47]. It must be noted that imperfect alignment of the XCT and CAD datasets during analysis could also lead to some of the under-print and over-print values observed in this study.

An additional two orthopaedic implant designs were evaluated to assess the adaptability of the proposed digital workflow for biomedical applications. Two orthopaedic implant designs were light-weighted with either a periodic TPMS lattice structure (gyroid) or a stochastic Voronoi lattice structure and manufactured in Ti6Al4V. Both the implant designs have a down-skin ratio <1 as shown in Figure 8, and both implants did print successfully. Both implants, however, have a higher volumetric over-print when compared to the successfully printed homogeneous lattice structures (except the FCC, which is considered a partial failure, and has the highest volumetric over-print when the standard deviation is considered, as shown in Figure 7) and Supplementary Information Figure 1. The higher over-print for the implant designs is partly related to the use of support structures at the bottom of the implants during prints, which could not be completely removed during the XCT versus CAD analysis. Additionally, an exact alignment of the highly complex implant designs to the XCT dataset is challenging, which could add to inaccuracies in the reported under-print and over-print values for the two designs. Regardless, the trend of the surface-based (TPMS) lattice design is seen to again outperform a strut-based stochastic Voronoi lattice design, in terms of both volumetric under-printing and over-printing.

While existing AM software, like Magics by Materialise (Belgium), have features to identify and calculate down-skin surfaces, the algorithms used in these commercial software packages are often a black box with few details available. The present digital work-flow acts to liberate this information through a stand-alone python script that can apply polydata to individual mesh elements of STL files. This approach to harvesting and assigning polydata, opens for future applications including utilizing data for machine learning and topology optimization pathways. The current down-skin ratio may act as a rule of thumb for manufacturability of lattices and complex parts. Further, the present study is an important step towards developing predictive machine learning models that allow for accurate estimations of final manufactured parts from preliminary CAD.

The current study thereby presents a novel approach to quantify and validate the relationship between down-skin surfaces for a given design and manufacturability of the designs manufactured using LPBF. The down-skin surface of multiple lattice types was evaluated using an image processing workflow to develop the down-skin ratio term as a means to quantify the printability of a given design. In this work, designs with down-skin ratios lesser than one are expected to print successfully with high dimensional fidelity between the CAD and printed coupons. This approach would help reduce the transition from design ideas to successful prints in LPBF.

5. Conclusions

The current study presents a novel digital evaluation workflow to determine the surface area and nature of down-skin regions on complex interconnected parts as well as a new approach for evaluating geometric fidelity as a function of volumetric over- and under-printing. Seven unique lattice structures were generated for down-skin evaluation. Six lattice structures were successfully manufactured in marging steel and evaluated for the relationship between down-skin and geometric fidelity. A higher percentage of down-skin surface area with a surface angle of 15 degrees or less and a down-skin ratio greater than one were indicators of poor geometric fidelity in the final parts. While down-skin evaluation is known to improve final part geometries, by characterizing the complex 3D interconnectivity of lattice structures, the robustness of the digital workflow was exhibited. The workflow was successfully applied to orthopaedic designs manufactured in Ti6Al4V to validate the adaptability to complex part geometries outside of individual unit cells. The use of multiple materials, marging steel and Ti6Al4V, strengthens the adaptability of the digital evaluation workflow by exhibiting that the down-skin ratio parameter is material agnostic, assuming pre-established print parameters for a given material. A known limitation exists with respect to evaluating the manufacturability of knife edge features and future work should look to address this challenge. These tools aim to assist in the evaluation of designs for manufacturability as well as serve to evaluate the success of final 3D printed parts using LPBF.

6. Acknowledgements

References

[1] J. Gardan, Smart materials in additive manufacturing: state of the art and trends, Virtual and Physical Prototyping 14 (1) (2019) 1–18.

[2] D. W. Rosen, Research supporting principles for design for additive manufacturing: This paper provides a comprehensive review on current design principles and strategies for am, Virtual and physical prototyping 9 (4) (2014) 225–232.

[3] W. J. Sames, F. List, S. Pannala, R. R. Dehoff, S. S. Babu, The metallurgy and processing science of metal additive manufacturing, International materials reviews 61 (5) (2016) 315–360.

[4] S. L. Sing, J. An, W. Y. Yeong, F. E. Wiria, Laser and electron-beam powder-bed additive manufacturing of metallic implants: A review on processes, materials and designs, Journal of Orthopaedic Research 34 (3) (2016) 369–385.

[5] M. McGregor, S. Patel, S. McLachlin, M. Vlasea, Architectural bone parameters and the relationship to titanium lattice design for powder bed fusion additive manufacturing, Additive Manufacturing 47 (2021) 102273.

[6] P. Mercelis, J.-P. Kruth, Residual stresses in selective laser sintering and selective laser melting, Rapid prototyping journal (2006).

[7] A. Ashby, G. Guss, R. K. Ganeriwala, A. A. Martin, P. J. DePond, D. J. Deane, M. J. Matthews, C. L. Druzgalski, Thermal history and high-speed optical imaging of overhang structures during laser powder bed fusion: A computational and experimental analysis, Additive Manufacturing 53 (2022) 102669.

[8] H. N. Wadley, Multifunctional periodic cellular metals, Philosophical Transactions of the Royal Society A: Mathematical, Physical and Engineering Sciences 364 (1838) (2006) 31–68.

[9] G. Dong, Y. Tang, Y. F. Zhao, A survey of modeling of lattice structures fabricated by additive manufacturing, Journal of Mechanical Design 139 (10) (2017) 100906.

[10] A. du Plessis, S. M. J. Razavi, M. Benedetti, S. Murchio, M. Leary, M. Watson, D. Bhate, F. Berto, Properties and applications of additively manufactured metallic cellular materials: A review, Progress in Materials Science (2021) 100918.

[11] E. Boccini, R. Furferi, L. Governi, E. Meli, A. Ridolfi, A. Rindi, Y. Volpe, Toward the integration of lattice structure-based topology optimization and additive manufacturing for the design of turbomachinery components, Advances in Mechanical Engineering 11 (8) (2019) 1687814019859789.

[12] C. Zhang, S. Wang, J. Li, Y. Zhu, T. Peng, H. Yang, Additive manufacturing of products with functional fluid channels: A review, Additive Manufacturing 36 (2020) 101490.

[13] S. Patel, M. McGregor, S. McLachlin, M. Vlasea, Digital manufacturing challenge: Rapid deployment of patient-specific prosthesis in emergency medicine enabled by additive manufacturing, Manufacturing Engineering 116 (12) (2021) 9–11.

[14] F. Calignano, Design optimization of supports for overhanging structures in aluminum and titanium alloys by selective laser melting, Materials & Design 64 (2014) 203–213.

[15] A. Triantaphyllou, C. L. Giusca, G. D. Macaulay, F. Roerig, M. Hoebel, R. K. Leach, B. Tomita, K. A. Milne, Surface texture measurement for additive manufacturing, Surface topography: metrology and properties 3 (2) (2015) 024002.

[16] J. C. Fox, S. P. Moylan, B. M. Lane, Effect of process parameters on the surface roughness of overhanging structures in laser powder bed fusion additive manufacturing, Procedia Cirp 45 (2016) 131–134.

[17] H. Chen, D. Gu, J. Xiong, M. Xia, Improving additive manufacturing processability of hard-to-process overhanging structure by selective laser melting, Journal of Materials Processing Technology 250 (2017) 99–108.

[18] A. Mulhi, S. Dehgahi, P. Waghmare, A. Qureshi, Dimensional assessment of uniformly periodic porosity primitive tpms lattices using additive manufacturing laser powder bed fusion technique, The International Journal of Advanced Manufacturing Technology (2022) 1–22.

[19] I. Echeta, X. Feng, B. Dutton, R. Leach, S. Piano, Review of defects in lattice structures manufactured by powder bed fusion, The International Journal of Advanced Manufacturing Technology 106 (2020) 2649–2668.

[20] D. Wang, Y. Yang, Z. Yi, X. Su, Research on the fabricating quality optimization of the overhanging surface in slm process, The International Journal of Advanced Manufacturing Technology 65 (9) (2013) 1471–1484.

[21] A. Charles, A. Elkaseer, U. Paggi, L. Thijs, V. Hagenmeyer, S. Scholz, Down-facing surfaces in laser powder bed fusion of ti6al4v: Effect of dross formation on dimensional accuracy and surface texture, Additive Manufacturing 46 (2021) 102148.

[22] V. Viale, J. Stavridis, A. Salmi, F. Bondioli, A. Saboori, Optimisation of downskin parameters to produce metallic parts via laser powder bed fusion process: an overview, The International Journal of Advanced Manufacturing Technology (2022) 1–24.

[23] H. Yeung, B. Lane, J. Fox, Part geometry and conduction-based laser power control for powder bed fusion additive manufacturing, Additive manufacturing 30 (2019) 100844.

[24] M. Shange, I. Yadroitsava, A. du Plessis, I. Yadroitsev, Roughness and near-surface porosity of unsupported overhangs produced by high-speed laser powder bed fusion, 3D Printing and Additive Manufacturing (2021).

[25] F. Cabanettes, A. Joubert, G. Chardon, V. Dumas, J. Rech, C. Grosjean, Z. Dimkovski, Topography of as built surfaces generated in metal additive manufacturing: A multi scale analysis from form to roughness, Precision Engineering 52 (2018) 249–265.

[26] A. Almalki, D. Downing, J. Noronha, J. Dash, B. Lozanovski, R. Tino, A. Alghamdi, M. Khorasani, M. Qian, M. Brandt, et al., The effect of geometric design and materials on section properties of additively manufactured lattice elements, The International Journal of Advanced Manufacturing Technology 126 (7-8) (2023) 3555–3577.

[27] G. Meyer, J. Musekamp, F. Göbel, F. Gardian, C. Mittelstedt, Manufacturability investigation of inclined alsi10mg lattice struts by means of selective laser melting, Manufacturing Letters 31 (2022) 101–105.

[28] C. G. Klingaa, M. K. Bjerre, S. Baier, L. De Chiffre, S. Mohanty, J. H. Hattel, Roughness investigation of slm manufactured conformal cooling channels using x-ray computed tomography, in: Proceedings of the 9th Conference on Industrial Computed Tomography (ICT 2019), Padova, Italy, 2019, pp. 13–15.

[29] T. Puttonen, Evaluation of metal lattice structures with x-ray micro-computed tomography: Dimensional accuracy and manufacturability, in: ASME International Mechanical Engineering Congress and Exposition, Vol. 84539, American Society of Mechanical Engineers, 2020, p. V006T06A015.

[30] N. Tanlak, D. F. De Lange, W. Van Paepegem, Numerical prediction of the printable density range of lattice structures for additive manufacturing, Materials & Design 133 (2017) 549–558.

[31] B. Lozanovski, D. Downing, R. Tino, P. Tran, D. Shidid, C. Emmelmann, M. Qian, P. Choong, M. Brandt, M. Leary, Image-based geometrical characterization of nodes in additively manufactured lattice structures, 3D Printing and Additive Manufacturing 8 (1) (2021) 51–68.

[32] K. Alrbaey, D. Wimpenny, R. Tosi, W. Manning, A. Moroz, On optimization of surface roughness of selective laser melted stainless steel parts: a statistical study, Journal of Materials Engineering and Performance 23 (2014) 2139–2148.

[33] E. E. Covarrubias, M. Eshraghi, Effect of build angle on surface properties of nickel superalloys processed by selective laser melting, Jom 70 (2018) 336–342.

[34] J. Zhang, A. Chaudhari, H. Wang, Surface quality and material removal in magnetic abrasive finishing of selective laser melted 316l stainless steel, Journal of manufacturing processes 45 (2019) 710–719.

[35] G. Tarakçı, H. M. Khan, M. S. Yılmaz, G. Özer, Effect of building orientations and heat treatments on alsi10mg alloy fabricated by selective laser melting: microstructure evolution, mechanical properties, fracture mechanism and corrosion behavior, Rapid Prototyping Journal 28 (8) (2022) 1609–1621.

[36] S. Patel, A. Rogalsky, M. Vlasea, Towards understanding side-skin surface characteristics in laser powder bed fusion, Journal of Materials Research 35 (15) (2020) 2055–2064.

[37] L. C. Wei, L. E. Ehrlich, M. J. Powell-Palm, C. Montgomery, J. Beuth, J. A. Malen, Thermal conductivity of metal powders for powder bed additive manufacturing, Additive Manufacturing 21 (2018) 201–208.

[38] T. M. Wischeropp, C. Emmelmann, M. Brandt, A. Pateras, Measurement of actual powder layer height and packing density in a single layer in selective laser melting, Additive Manufacturing 28 (2019) 176–183.

[39] A. Jones, M. Leary, S. Bateman, M. Easton, Effect of surface geometry on laser powder bed fusion defects, Journal of Materials Processing Technology 296 (2021) 117179.

[40] G. A. Adam, D. Zimmer, Design for additive manufacturing—element transitions and aggregated structures, CIRP Journal of Manufacturing Science and Technology 7 (1) (2014) 20–28.

[41] Z.-D. Zhang, O. Ibhadode, U. Ali, C. F. Dibia, P. Rahnama, A. Bonakdar, E. Toyserkani, Topology optimization parallel-computing framework based on the inherent strain method for support structure design in laser powder-bed fusion additive manufacturing, International Journal of Mechanics and Materials in Design 16 (2020) 897–923.

[42] A. Khobzi, F. F. Mehr, S. Cockcroft, D. Maijer, S. L. Sing, W. Y. Yeong, The role of block-type support structure design on the thermal field and deformation in components fabricated by laser powder bed fusion, Additive Manufacturing 51 (2022) 102644.

[43] Y. Liu, Y. Yang, D. Wang, Investigation into the shrinkage in z-direction of components manufactured by selective laser melting (slm), The International Journal of Advanced Manufacturing Technology 90 (2017) 2913–2923.

[44] J. K. Veetil, M. Khorasani, A. Ghasemi, B. Rolfe, I. Vrooijink, K. Van Beurden, S. Moes, I. Gibson, Build position-based dimensional deviations of laser powder-bed fusion of stainless steel 316l, Precision engineering 67 (2021) 58–68.

[45] V. Chahal, R. M. Taylor, A review of geometric sensitivities in laser metal 3d printing, Virtual and Physical Prototyping 15 (2) (2020) 227–241.

[46] L. Zhang, Y. Li, H. Zhu, Prediction and optimization of dimensional accuracy of inclined structures fabricated by laser powder bed fusion, Journal of Manufacturing Processes 81 (2022) 281–289.

[47] Z. M. Taib, W. S. W. Harun, S. A. C. Ghani, M. Rashid, M. A. Omar, H. Ramli, Dimensional accuracy study of open cellular structure cocrmo alloy fabricated by selective laser melting process, Advanced Materials Research 1133 (2016) 280.